applied sciences

MDPI

Article

Impact of Intracavity Power Variations toward Ultrashort Pulse Generation

Ahmad Fauzi Abas [1,*], Kuen Yao Lau [2], Yahya Mohammed Al-Moliki [1], Yosef Taher Aladadi [1], Mohammed Thamer Alresheedi [1] and Mohd Adzir Mahdi [3]

[1] Department of Electrical Engineering, College of Engineering, King Saud University, P.O. Box 800, Riyadh 11421, Saudi Arabia
[2] State Key Laboratory of Modern Optical Instrumentation, College of Optical Science and Engineering, Zhejiang University, Hangzhou 310027, China
[3] Wireless and Photonics Networks Research Centre, Faculty of Engineering, Universiti Putra Malaysia, Serdang 43400, Selangor, Malaysia
* Correspondence: aabas@ksu.edu.sa

Abstract: This study demonstrates a passive mode-locked erbium-doped fiber laser with a graphene nanoplatelet-saturable absorber (GNP-SA) that generates ultrashort pulses within femtosecond pulse duration. The GNP-SA is fabricated via a direct transfer approach by mechanically exfoliated graphene on a fiber ferrule. Its characteristics include 0.8% modulation depth, 8.7 MW/cm^2 saturation fluence, and 36.8% absorbance. The quality of ultrashort pulses is studied with a variation of intracavity circulating powers that is controlled through an optical coupler. By changing the light intensity in the cavity, the optical amplification property in the erbium-doped fiber is also impacted. The increment of the output coupling ratio increases the population inversion in the active gain medium, which leads to the change of lasing wavelength from 1558 to 1532 nm. Using a 50% output coupling ratio, the fiber laser generates 960 fs pulse duration, 11.08 MHz repetition rate, and 6.05 mW output power. This study contributes to the understanding of oscillating light behavior while changing its intracavity power that affects the optical amplification properties.

Keywords: graphene; ultrashort pulse; erbium

Citation: Abas, A.F.; Lau, K.Y.; Al-Moliki, Y.M.; Aladadi, Y.T.; Alresheedi, M.T.; Mahdi, M.A. Impact of Intracavity Power Variations toward Ultrashort Pulse Generation. *Appl. Sci.* **2023**, *13*, 4087. https://doi.org/10.3390/app13074087

Academic Editor: Detlef Kip

Received: 26 February 2023
Revised: 19 March 2023
Accepted: 20 March 2023
Published: 23 March 2023

1. Introduction

Fiber lasers have been rigorously investigated since the invention of erbium-doped fibers [1]. Rare-earth doped fibers are a highly efficient gain medium that provides excellent beam quality. Another advantage of fiber lasers is the scalability of their output power with an innovative design of double-clad fibers for multimode pumping schemes [2,3]. Owing to these advantages, fiber lasers have been demonstrated in various applications, such as high power [4,5], wide tunability [6,7], multi-wavelength [8,9], and ultrashort pulse applications.

The most sought-after trait of mode-locked ultrashort pulse laser systems in material processing applications is their capability to generate pulses at very high intensity with an extremely short interaction time. Not only would this allow materials such as metals [10] and ceramics [11] to be machined with exceptional precision, transparent and thermally sensitive media such as biopolymers [12] and glass [13] can be processed, too. To generate ultrashort optical pulses, there are two common techniques: active and passive mode-locking. For the active mode-locking method, an optical modulator is normally used to control the generated pulse durations [14,15]. Its operation relies on the response time of the optical modulator to modulate the oscillating light in the cavity as a result of longer pulse durations. In addition, the electronic driver must be synchronized with the round-trip time of the pulse, which creates another challenge for this technique.

The passive mode-locking technique is a popular choice as compared with active mode-locking techniques as they do not require external electronic components. In passive

mode-locking, a nonlinear optical device called a saturable absorber (SA) is deployed in the cavity to generate ultrashort pulses. Optical pulses originated from noise fluctuations in the laser cavity. A noise spike of sufficient intensity will begin to saturate the absorber, reducing its losses. The noise spike will be further amplified in subsequent round trips, and the increased intensity will saturate the losses until a stable train of pulses eventually forms. Within these pulses, the central peak intensity saturates the SA more strongly than the pulse wings, leading to a further reduction in the pulse duration. The absorption of the SA decreases with the increment of input optical intensity.

Material-based fiber SAs have attracted lots of attention due to their versatility of full integration with other optical components in fiber laser designs. The early concept of this SA was proposed by Set et al. [16] utilizing carbon nanotubes (CNTs). The proposed device incorporated a CNT layer between two substrates; however, a few bulk optics were still required to focus the light beam for effective interaction. To rectify the requirement of optical alignment using bulk optics, CNTs can be embedded with other polymers to function as a SA in the form of a thin film [17]. For this setup, the CNT thin film can be sandwiched between two fiber ferrules eliminating the requirement of optical alignments. This approach can also be applied to graphene as the nonlinear material in polyvinyl acetate [18] and polyvinyl alcohol [19] as the host polymer. Placing a graphene/polymer thin film on the fiber ferrule is proven to be a simple approach, as demonstrated in the 1.56 μm [20–22] and the 2.1 μm [23]. In addition to graphene, various materials have been demonstrated to generate ultrashort pulses using this technique: zinc phthalocyanine [24], titanium carbide MXene [25], gallium antimonide [26], zirconium disulfide [21], alpha ferric oxide [27], and lanthanum hexaboride [28].

In addition, another technique of optical deposition is also explored to attach graphene directly to the fiber ferrule surface [29]. This approach was first reported based on the CNT material [30,31]. The optical deposition relies on the interaction between the injected light and material-dispersed solution. In this technique, by dipping the cleaved fiber into the material-based solution while injecting laser light, the material is attracted to the fiber core. The thickness of the material on the fiber core can be controlled by adjusting its deposition time and the intensity of laser light [30].

Last but not least, the simplest method of depositing graphene is found by the breakthrough discovery of peeling off graphite layer-by-layer using Scotch tape [32,33]. This discovery is also known as mechanical exfoliation which can be applied directly in fabricating graphene-based SA using fiber ferrules [34]. The fabricated multi-layered graphene SA produced about 3.2 ps pulse duration based on the estimation of the transform-limited soliton theorem. Besides graphene, this technique has been utilized for other materials; black phosphorus [35,36], platinum diselenide [37], rhenium disulfide [38], molybdenum disulfide [39], and graphene/indium selenide [40]. Mechanical exfoliation can also be adopted with mirror-based SA that has been incorporated in fiber laser setups that cover 2.8 μm (graphene [41] and indium selenide [42]) and 3.5 μm (black phosphorus [43] and single-walled CNTs [44]).

Our group has also successfully developed multi-layered graphene SA on fiber ferrule using this technique [45,46]. Previous works focused on the ultrashort pulse generation in a single- [45] and a dual-wavelength laser system [46]. In this work, we demonstrate the performance of soliton mode-locking generated from graphene nanoplatelet (GNP) as the SA by changing intracavity losses. The GNP in bulk form is transferred to a fiber ferrule, and then it is mechanically exfoliated. The fabricated GNP-SA is tested in a ring cavity erbium-doped fiber laser (EDFL) with a variation in output coupling ratios from 10% to 50%. The feedback reflectivity determines the population inversion level of the active gain medium. As a result, optical amplification in the gain medium becomes dynamic, which dictates the ultrashort pulse performance.

2. Graphene Nanoplatelet Powder

The preparation of GNP powder has been described in [47]. The expanded graphite (3772, Asbury Carbons, Inc., Asbury, NJ, USA) is thermally exfoliated for ten seconds at 950 °C. To exfoliate expanded graphite, 0.1 g of the expanded fluffy powder is steeped for 24 h in 100 mL of a mixture containing sulfuric acid ($V(H_2SO_4)$) and nitric acid ($V(HNO_3)$). The treated expanded graphite is then rinsed ten times in deionized water using the centrifuge technique to eliminate extra acids. To exfoliate further, the processed expandable graphite is ultrasonicated utilizing a probe sonicator (QSonica Q700) in ethanol solution (0.1 mg/mL). The sonicated sample is centrifuged at 5000 rpm, and the residue is oven-dried at 60 °C for 12 h to produce GNP powders.

Figure 1 compiles the material characterization of the synthesized GNP powder. Figure 1a depicts the absorption spectrum of the GNP powder using a Shimadzu UV-1601 UV-visible spectrophotometer. The conventional graphite material's p-plasmon activation provides a maximum absorbance of 260 nm [47]. Furthermore, the gapless material transition of graphene has extensive absorbance at 270 nm [47]. The absorption peak of GNP powder seen at 267 nm, based on experimental data, reveals that this substance is formed of many layers. As shown in Figure 1b, a Renishaw inVia Raman microscope with laser excitation at 532 nm is employed to obtain the Raman spectrum of GNP powder. The GNP powder is determined to have a multi-layered structure since the I_{2D}/I_G ratio is less than two (0.53) [48].

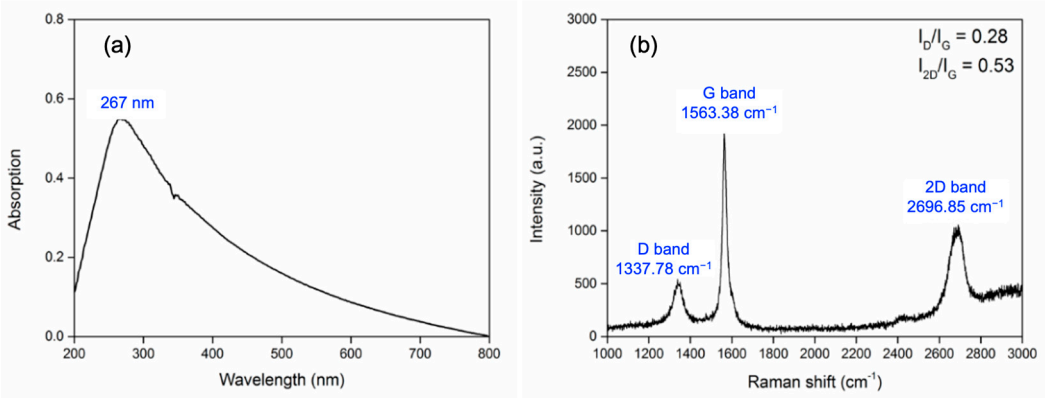

Figure 1. (**a**) UV–VIS spectrum and (**b**) Raman spectrum of GNP powder.

3. Saturable Absorber Characteristics

To fabricate GNP-SA, the mechanical exfoliation method was chosen, as illustrated in Figure 2. This technique has been elaborated on in our previous work [45]. In this technique, a clean fiber channel/physical contact (FC/PC) connector is first coated with an index-matching gel. Then it is dipped in a bulk amount of graphene powder and after pulling out the FC/PC connector, a small amount of graphene nanoplatelet is attached on a fiber ferrule with the help of an adhesive provided by the index matching gel, as shown in Figure 2. To minimize its thickness, Scotch tape is utilized to remove the crumpled graphene layer by layer. This process is repeated a few times until a very thin layer of graphene is seen on the fiber ferrule. Then, it is connected to another FC/PC connector using a fiber adapter to assemble a GNP-SA.

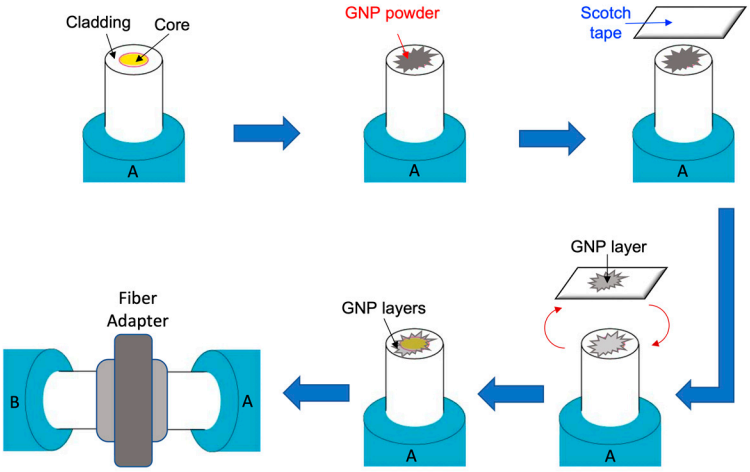

Figure 2. Fabrication of GNP-SA, A represents a FC/PC pigtail which the deposited GNP and B is another FC/PC pigtail for the mating process.

First, it is important to understand the optical characteristics of the fabricated GNP-SA. For optical transmission measurements, a broadband amplified spontaneous emission (ASE) source (Amonics model ALS-CL-17-B-SC) is applied. For the measurement of the reference spectrum, the ASE source is connected to a Yokogawa AQ6370B optical spectrum analyzer (OSA) with a resolution bandwidth set at 0.02 nm. The fabricated GNP-SA is then positioned between the ASE source and the OSA. The transmission spectrum is measured and then compared with the reference. Figure 3 depicts the transmission of the GNP-SA from 1525 to 1575 nm. This transmission loss includes the insertion loss that occurs between the fiber ferrules and the GNP material. For this work, the transmission was more than 60%, which translates to a maximum loss of 40% only in the entire wavelength range.

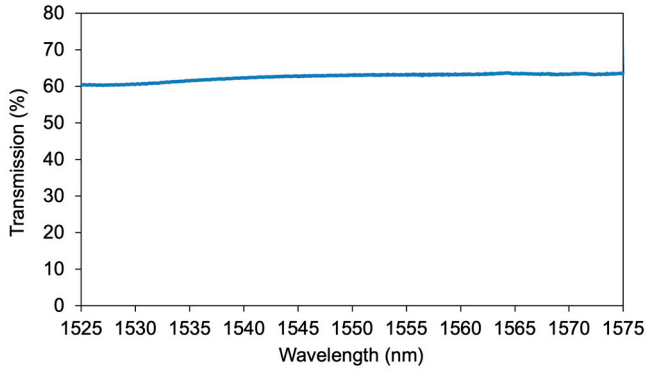

Figure 3. Transmission loss of GNP-SAs across conventional band (C-band) wavelength region.

For nonlinear absorption measurement, a balanced twin detector approach was employed, as depicted in Figure 4. The experimental setup consists of a pulsed laser source (PLS) with a center wavelength of 1560 nm, a pulse repetition rate of 250 MHz, and pulse duration of 117 fs. A variable optical attenuator (VOA) is used to vary the PLS power as the input variable. A 50/50 optical coupler divides the optical route evenly between path A and path B. Between the VOA and the 50/50 optical coupler, an isolator is inserted to prohibit any back-reflected signal from propagating to the PLS. Path A is utilized to measure the reference power, while path B is meant to measure the power-dependent transmission. The GNP-SA is placed in path B as the device is sensitive to the input power variation. The optical power of both signals is measured using two identical optical power meters (OPMs), namely OPM1 and OPM2.

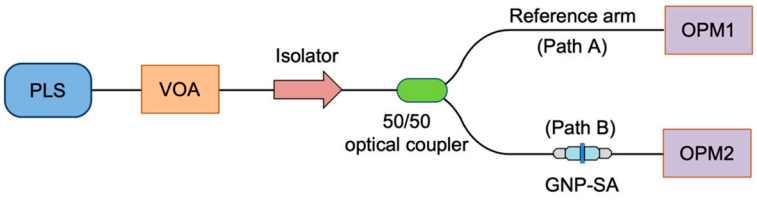

Figure 4. Nonlinear saturable absorbance of SA measurement setup.

The nonlinear absorption curve of GNP-SA is depicted in Figure 5. In accordance with the progression of the curve, the absorbance declines rapidly at first, then slowly towards the saturation regime. To determine the characteristics of a SA, the nonlinear saturable absorption equation [49] was chosen as follows:

$$\alpha(I) = \frac{\alpha_s}{1 + \frac{I}{I_{sat}}} + \alpha_{ns}, \tag{1}$$

where $\alpha(I)$ is the intensity-dependent absorption, α_s is the saturable absorbance (modulation depth, MD), I is the laser intensity, I_{sat} is the saturation intensity, and α_{ns} is the non-saturable absorbance. Figure 5 depicts the measured nonlinear absorption of the GNP-SA with its curve fitting from Eqn. 1. From the analysis, the GNP-SA produces a modulation depth of 0.8%, non-saturable absorbance of 36.8%, and saturation intensity of 8.7 MW/cm^2.

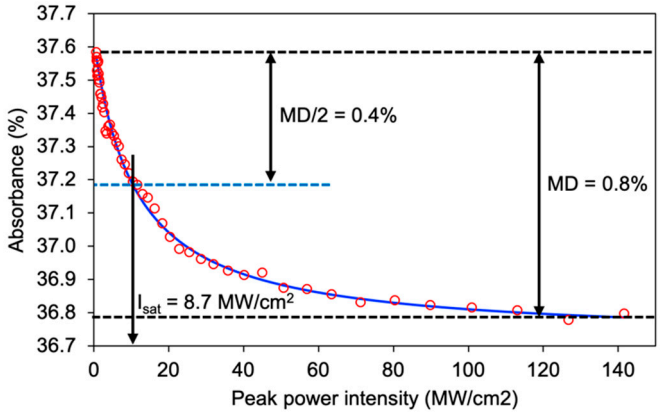

Figure 5. Nonlinear saturable absorbance properties of GNP-SA.

4. Experimental Setup

Figure 6 depicts the experimental setup of a mode-locked EDFL using the homemade GNP-SA. A 975 nm pump laser diode (LD) with a maximum power of 99 mW was employed as the excitation source. This pump light is coupled to a 5 m long erbium-doped fiber (EDF) via a 980/1550 nm wavelength division multiplexer (WDM). The EDF has a 5.2 dB/m absorption coefficient at 1530 nm, 0.19 numerical aperture, and 8.5 mm mode field diameter. The GNP-SA is positioned between two isolators (ISOs), namely ISO-1 and ISO-2. This arrangement is critical to ensure unidirectional light propagation. In addition, by having two isolators, back-reflections from the GNP-SA can be avoided. The presence of back-reflected light is generated at the interface between fiber ferrule and GNP material due to the refractive index difference. By using this arrangement, multiple reflections that degrade laser stabilities can be completely rectified. A polarization controller (PC) is inserted in the laser cavity to regulate the polarization state and optimize cavity birefringence impacts.

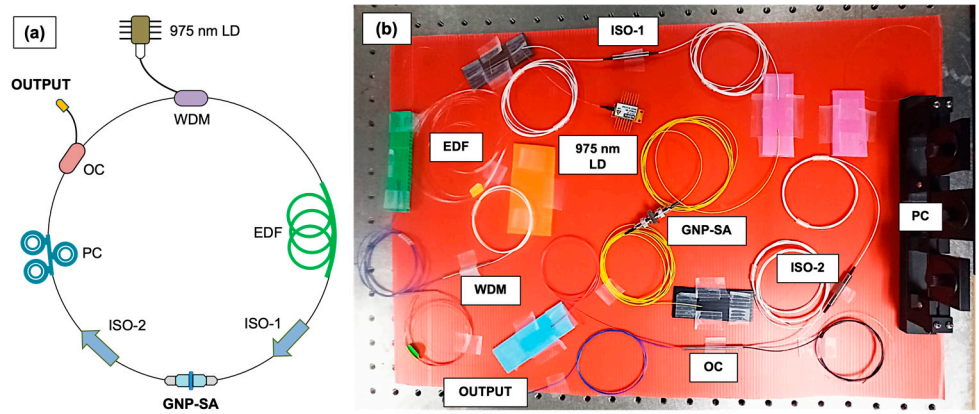

Figure 6. Experimental setup of mode-locked EDFL with GNP-SA (**a**) schematic diagram and (**b**) actual layout.

The output of the PC was coupled to an optical coupler (OC) which was the variable parameter in this study. Five different sets of OCs were tested in the laser cavity, namely 10/90, 20/80, 30/70, 40/60, and 50/50. The variable output coupling ratio was determined by changing the output arm for all couplers. Therefore, there were two sets of output coupling ratios for each OC except the 50/50 OC. The laser cavity consisted of three types of optical fibers: 8.4 m length of Corning SMF-28, 1 m length of Corning Hi-1060 fiber, and 5 m length of Lucent Technologies HP980 EDF. The dispersion coefficient, β_2 at 1550 nm for the SMF-28, Hi-1060 SMF, and EDF were -22, -7 and 23 ps^2/km, respectively. The total group velocity dispersion of the laser setup was -0.077 ps^2, which confirms its operation in the anomalous dispersion regime.

5. Pulse Laser Performance

In this work, nine sets of experiments were conducted to determine the efficiency of generating ultrashort pulses. From these, four sets of experiments that used 60%, 70%, 80% and 90% arms as the output coupling ratio cannot produce stable lasers. Therefore, only five sets of experiments that generated stable lasers are analyzed throughout this report. Figure 7a shows the laser output for a 30% output coupling ratio at 99 mW pump power as an example of the analysis. The central wavelength of the laser is about 1557.5 nm, which indicates moderate population inversion of the erbium system. Its spectral bandwidth of 3.78 nm is obtained from this arrangement. It is important to note that the laser spectrum consists of symmetrical Kelly sidebands as the indication of mode-locked pulse formation in the cavity. We also confirm this pulse phenomenon with the presence of a pulse train in the oscilloscope that is measured simultaneously. Figure 7b depicts the central lasing wavelength and associated spectral bandwidth from 10% to 50% output coupling ratio. The pulse formation is also confirmed by the appearance of a pulse train in the oscilloscope, as previously explained.

For the analysis of spectral bandwidth, the largest value of 3.78 nm is observed using a 30% output coupling ratio. While the lowest value of 2.31 nm is recorded using a 10% output coupling ratio. Furthermore, the spectral bandwidth value is also decreased to 2.66 nm. The lasing bandwidth is associated with the strength of the soliton mode-locking mechanism that is influenced by the balance of dispersion and nonlinearity. However, the former factor is almost negligible because the total length and type of fiber are kept constant throughout the experiment. Thus, the latter factor is the main contributor to this observation, which can be explained by the dynamics of light amplification in the EDF. In this case, the 30% output coupling ratio is the optimum condition to harness the widest spectral bandwidth that leads to the shortest pulse formation.

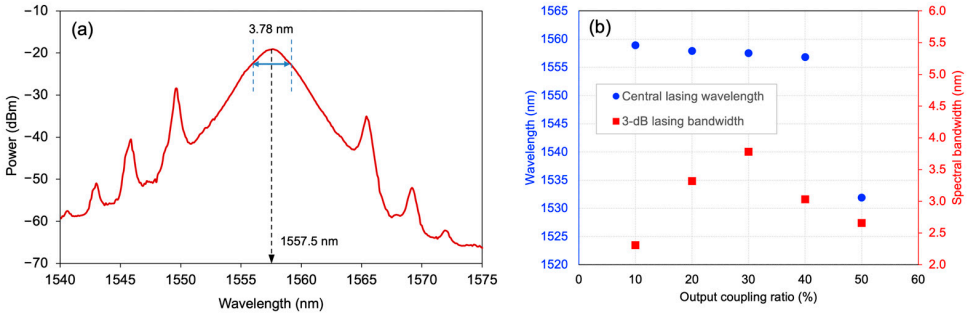

Figure 7. (**a**) Optical spectrum of EDFL generated by GNP-SA using a 30% output coupling ratio and (**b**) central wavelength and spectral bandwidth for different output coupling ratios.

To explain the lasing wavelength properties, it is important to relate this phenomenon with the condition of population inversion level in the EDF. Based on the Giles parameter in the classical optical amplifier model, the gain coefficient $G_c(\lambda)$ of the EDF is governed by the following equation [50]:

$$G_c(\lambda) = \eta(g(\lambda) + \alpha(\lambda)) - \alpha(\lambda) \quad (2)$$

where η is the population inversion factor, $g(\lambda)$ and $\alpha(\lambda)$ are the wavelength-dependent emission and absorption coefficient, respectively. The population inversion value is the key parameter to determine the peak gain that determines the lasing wavelength in a cavity. To relate between the gain coefficient and intracavity power associated to this work, a schematic diagram is drawn, as illustrated in Figure 8a. To simplify, we present two conditions of intracavity power: low (X) and high (Y). Similarly, in this case, X and Y represent high and low output coupling ratios, respectively.

Referring to Figure 6, the EDF is injected by the 0.98 µm pump light in a forward-pumping scheme. The circulating light (1.53–1.56 µm) and 0.98 mm pump light propagate in the same direction at the EDF input as illustrated in Figure 8b. The pump energy is absorbed at the input end of the EDF, and most of the electrons are excited to a higher energy level. However, the number of photon counts for X and Y are different. For Y, since the intracavity power is larger, more photons are generated through stimulated emission processes. Under this condition, more energy at the pump light is absorbed. Towards the end of EDF, the pump energy is absorbed faster which leads to a greater length of pump depletion region represented by the shaded area. Under this situation, signal re-absorption occurs as a result of lesser energy in the wavelength range of 1.53–1.56 µm. In this scenario, the EDF is operated in deep saturation level (low population inversion level). In comparison to X, the signal re-absorption process is lower since the pump depletion region is shorter. The EDF saturation level is also lower (high population inversion level) and results in larger output powers for the 1.53–1.56 µm light.

The population inversion factor plays a critical role in determining the lasing wavelength. It is subjected to the gain profile of the material used in the laser cavity. To illustrate its impact, Figure 8c depicts the normalized EDF gain using different population inversion values. The emission and absorption coefficients are obtained from the optical fiber manufacturer. From Equation (2), the value of the population inversion is varied. These values are not accurate and are purposely chosen to elaborate the lasing wavelength phenomenon. As shown in Figure 8c, as the intracavity power increases, the population inversion level decreases. Based on Equation (2), the estimated value of the population inversion level is in the range of 58–65%. When the population inversion is around 65%, the lasing wavelength occurs at about 1530 nm (blue arrow), the highest peak of the EDF gain. When the population inversion level reduces to 58%, the lasing wavelength shifts to longer wavelengths. The lasing wavelength takes place in the range between 1556 and 1560 nm, represented by the green and red arrows. In relation to the experimental findings (Figure 7), a lasing wavelength longer than 1556 nm is recorded for all output coupling ratios smaller than 50%.

There is an increment trend of the lasing wavelength when the output coupling ratio is decreased; the population inversion level is also decreased. The longest lasing wavelength of 1558.9 nm is recorded using a 10% output coupling ratio. The lasing wavelength of 1531.9 nm is attained using a 50% output coupling ratio (high population inversion level). These results indicate that by changing the feedback reflectivity (intracavity power), the population inversion can be adjusted accordingly.

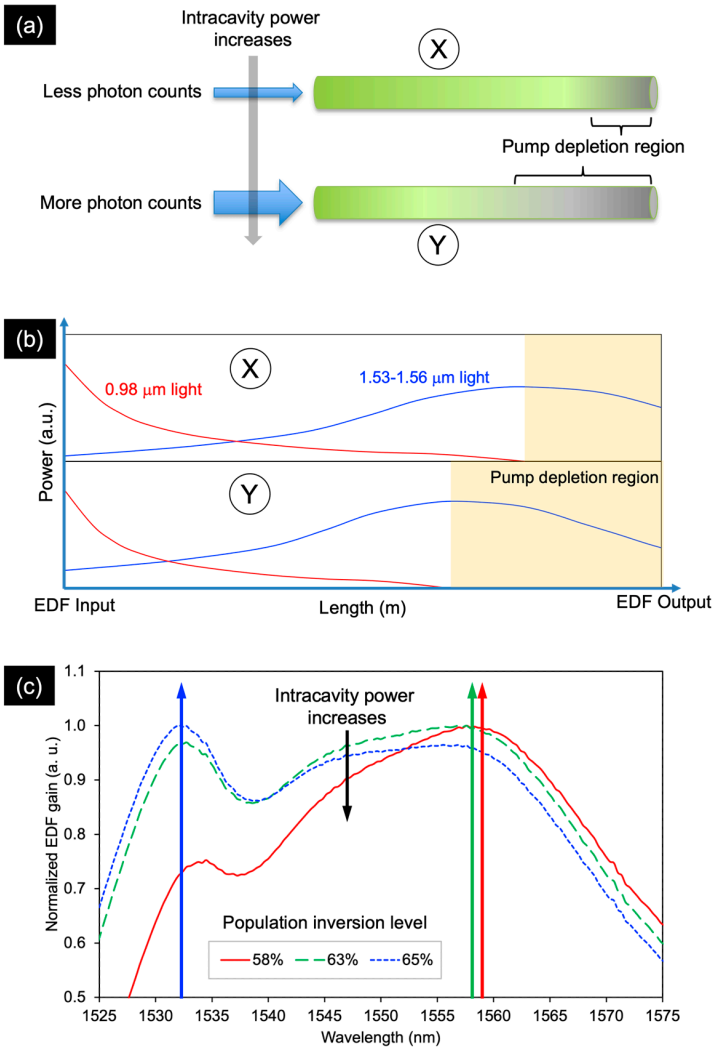

Figure 8. (**a**) Schematic diagram of light propagation in the EDF with variation of intracavity powers, (**b**) pump and signal light propagation profile in the EDF and (**c**) the normalized EDF gain with different population inversion levels. X and Y represent the condition of high and low output coupling ratios, respectively.

The measured pulse train in the time domain using the 30% output coupling ratio is shown in Figure 9a. For this measurement, the pump power of 975 nm LD is set at 99 mW. The oscilloscope trace indicates a clean pulse train with 89.37 ns time separation between subsequent pulses. In fact, there is no indication of the presence of other soliton phenomena, such as harmonic and multiple pulses. The round-trip time of 89.37 ns represents a pulse repetition rate of 11.19 MHz which is in agreement with the total cavity length of 14.4 m. Figure 9b portrays the value of the repetition rate for all output coupling ratios from 10% to 50%. The repetition rate value fluctuates between 11.08 and 11.19 MHz, which is considered almost constant. This small variation is caused by small differences in the fiber length by changing the optical coupler.

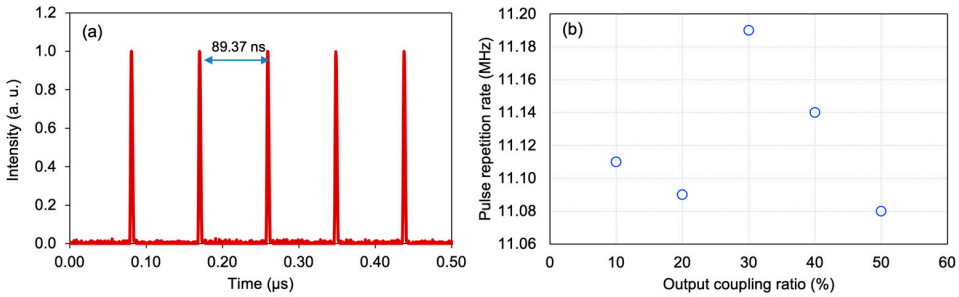

Figure 9. Pulse repetition rate of EDFL with GNP-SA; (**a**) oscilloscope trace of the output pulse for 30% and (**b**) different output coupling ratio values.

Figure 10a illustrates the frequency domain trace obtained from a radio frequency (RF) spectrum analyzer using the 30% output coupling ratio. The RF spectrum indicates a stable pulse train with a power extinction ratio (PER) of 58.3 dB. This value occurs at 11.19 MHz fundamental frequency, which is matched with the value deduced from the oscilloscope trace from Figure 9a. For other output coupling ratios, the value of PER at the fundamental frequency is more than 53 dB, as shown in Figure 10b.

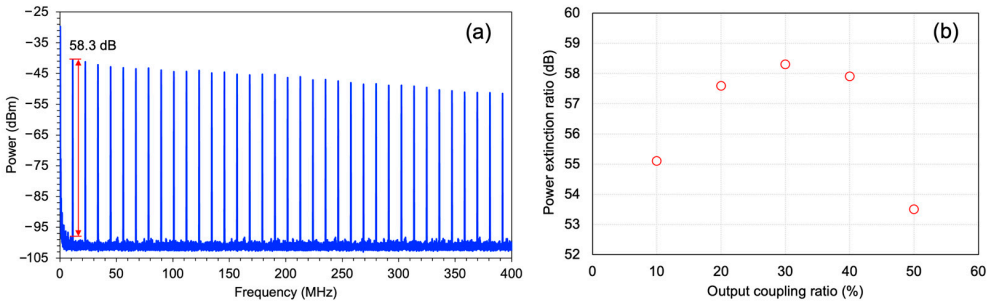

Figure 10. (**a**) RF spectrum using the 30% output coupling ratio and (**b**) the PER value at the fundamental frequency for different output coupling ratio values using 99 mW pump power.

As illustrated in Figure 11a, the pulse duration of the 30% output coupling ratio at 99 mW pump power is evaluated. First, the pulse duration is determined by measuring the value of its full width of half maximum (FHWM) pulse duration. In this experiment, the FWHM value is 1250 fs. The pulse is fitted with the sech^2 fitting curve, which has a 0.648 decorrelation factor. Based on this fitting, the actual pulse duration is 810 fs after multiplying with this decorrelation factor. The same analysis is applied to other output coupling ratios, and their pulse duration values are presented in Figure 11b. The slowest pulse occurs using a 10% output coupling ratio; however, this condition is already near to its transform-limited pulse by referring to the value of its time-bandwidth product (TBP) of 0.319. Although a 30% output coupling ratio produces the shortest pulse, its TBP value is recorded at 0.378. This indicates that the generated pulse is slightly chirped.

Figure 12a,b depict the evolution of average output power and pulse energy with respect to pump power at different output coupling ratios. In general, the average output power increases in tandem with pump power after the threshold power. The repetition rate of the pulse is almost constant; therefore, the pulse energy is also directly proportional to the pulse power. Figure 12c summarizes the value of the average output power and pulse energy at the maximum pump power of 99 mW. According to experimental results, the average output power rises as the output coupling ratio increases. This is owing to the increment of the OC loss as a result of the photon count reduction at the entrance of the EDF (after the WDM, refer to Figure 6). Since the pump power is maintained at 99 mW, the population inversion level in the EDF is also increased due to the reduction in the photon count. This is also translated to the reduction in gain saturation in the EDF, as explained previously. At the highest output coupling ratio of 50%, the amplification occurs in a longer

section transversely; the pump depletion is the lowest compared with the other OCs. In this case, the pump depletion is inversely proportional to the increment of the output coupling ratio (refer to Figure 8b). For the situation of pump depletion, the amplified signal is reabsorbed in the region where the photon count number at signal wavelength is greater than that of pump wavelength. Therefore, the localized signal power along the EDF depends on the photon count number at the entrance of the EDF. The dynamic of this phenomenon leads to the quality of the pulse generated from this laser cavity.

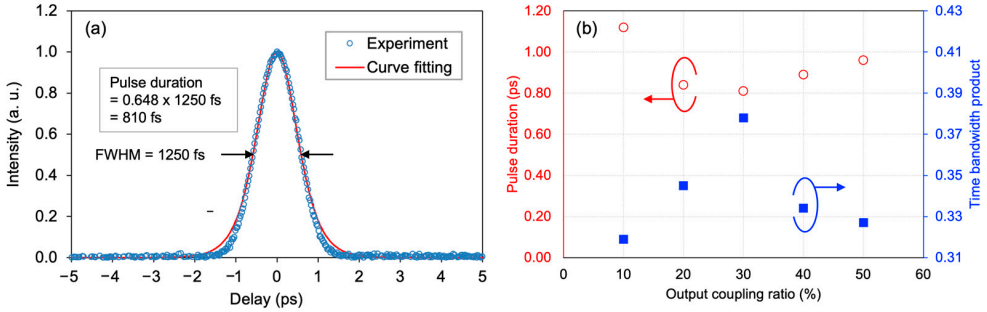

Figure 11. Pulse duration of EDFL with GNP-SA; (**a**) autocorrelator trace of the output pulse using a 30% output coupling ratio and (**b**) the pulse duration value of different output coupling ratio values.

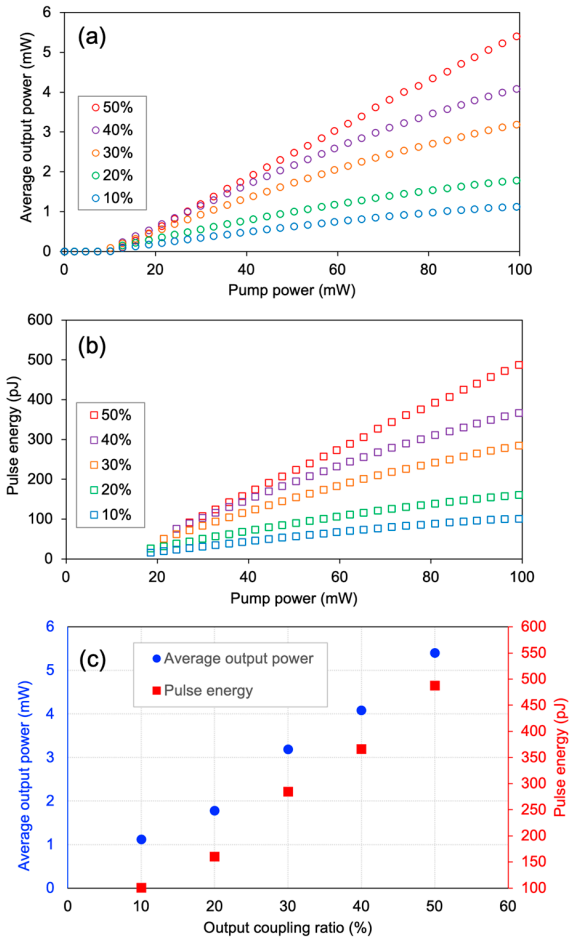

Figure 12. (**a**) Power and (**b**) energy development of EDFL with GNP-SA for different output coupling ratio values. (**c**) The value of output power and energy at the maximum pump power for different output coupling ratios.

6. Conclusions

In this work, we have investigated the performance of an ultrashort pulse generated by GNP-SA in mode-locked EDFL with the variation of output coupling ratio from 10% to 50%. The preparation of GNP-SA is made using the simple deposition method of mechanical exfoliation. To fabricate the SA, the bulk material of the graphene nanoplatelet is transferred onto a fiber ferrule with the help of the index-matching gel. The thickness of the GNP is minimized by layer-by-layer peeling using Scotch tape until a very thin layer of GNP is formed on the fiber ferrule. The fabricated GNP-SA has a 0.8% modulation depth, an 8.7 MW/cm^2 saturation fluence, and a 63.2% transmission. The insertion of GNP-SA into a ring-cavity EDFL is responsible for ultrashort pulse generations. The property of lasing oscillation is dependent on the intracavity powers. For an output coupling ratio of less than 50%, the lasing wavelength is observed in the long wavelength range within 1557–1559 nm. This indicates that the EDFL operates at a low population inversion level. When the output coupling ratio is increased from 40% to 50%, the lasing wavelength is switched from 1556.8 nm to 1531.9 nm. The intracavity power is decreased, and therefore, the number of signal photons at the entry point of EDF is also reduced. In this situation, the saturation level of optical amplification in the active gain medium is also reduced. As a result, the output power is increased. The maximum output power of 6.05 mW is obtained using a 50% output coupling ratio, and the shortest pulse duration of 810 fs is achieved using a 30% output coupling ratio. From this work, the design of the fiber laser setup is highly influenced by the availability of the signal photon count at the input of EDF, which determines the optical amplification dynamics in the active gain medium.

Author Contributions: Conceptualization, A.F.A., K.Y.L. and M.A.M.; methodology, A.F.A., K.Y.L., M.T.A. and M.A.M.; software, K.Y.L.; validation, A.F.A., K.Y.L. and M.A.M.; formal analysis, A.F.A., K.Y.L., Y.M.A.-M., Y.T.A., M.T.A. and M.A.M.; investigation, A.F.A., K.Y.L., Y.M.A.-M., Y.T.A., M.T.A. and M.A.M.; resources, A.F.A., M.T.A. and M.A.M.; data curation, K.Y.L.; writing—original draft preparation, K.Y.L. and Y.M.A.-M.; writing—review and editing, A.F.A., K.Y.L., Y.M.A.-M., Y.T.A., M.T.A. and M.A.M.; visualization, A.F.A., K.Y.L., M.T.A. and M.A.M.; supervision, A.F.A., M.T.A. and M.A.M.; project administration, A.F.A., M.T.A. and M.A.M.; funding acquisition, A.F.A. and M.T.A. All authors have read and agreed to the published version of the manuscript.

Funding: National Plan for Science, Technology and Innovation (MAARIFAH), King Abdulaziz City for Science and Technology, Kingdom of Saudi Arabia, award number 3-17-09-001-0007.

Data Availability Statement: Data sharing is not applicable to this article.

Acknowledgments: This project was funded by the National Plan for Science, Technology and Innovation (MAARIFAH), King Abdulaziz City for Science and Technology, Kingdom of Saudi Arabia, Award Number 3-17-09-001-0007.

Conflicts of Interest: The authors declare no conflict of interest.

References

1. Mears, R.J.; Reekie, L.; Jauncey, I.M. High-power tunable erbium-doped fiber laser operating at 1.55 μm. In Proceedings of the Conference on Lasers and Electro-Optics, Baltimore, MD, USA, 26 April–1 May 1987; pp. 122–123. Available online: https://opg.optica.org/abstract.cfm?uri=cleo-1987-WD3 (accessed on 16 February 2023).
2. Furusawa, K.; Malinowski, A.; Price, J.H.V.; Monro, T.M.; Sahu, J.K.; Nilsson, J.; Richardson, D.J. Cladding pumped Ytterbium-doped fiber laser with holey inner and outer cladding. *Opt. Express* **2001**, *9*, 714–720. [CrossRef] [PubMed]
3. Durán-Sánchez, M.; Reyes-Mora, A.; Pottiez, O.; Rodríguez-Morales, L.A.; Armas-Rivera, I.; Bello-Jiménez, M.; Alaniz-Baylón, J.; Ibarra-Escamilla, B. Dark rectangular pulses from a dumbbell-shaped mode-locked double-clad Er:Yb laser. *IEEE Photon. Technol. Lett.* **2022**, *34*, 1147–1150. [CrossRef]
4. Zeng, L.; Yang, H.; Xi, X.; Ye, Y.; Huang, L.; Yang, B.; Zhang, H.; Yan, Z.; Wang, X.; Pan, Z.; et al. Optimization and demonstration of 6 kW oscillating-amplifying integrated fiber laser employing spindle-shaped fiber to suppress SRS and TMI. *Opt. Laser Technol.* **2023**, *159*, 108903. [CrossRef]
5. Klenke, A.; Jauregui, C.; Steinkopff, A.; Aleshire, C.; Limpert, J. High-power multicore fiber laser systems. *Prog. Quantum Electron.* **2022**, *84*, 100412. [CrossRef]

6. ChmielowskI, P.; Nikodem, M. Widely tunable continuous-wave fiber laser in the 1.55–1.8 μm wavelength region. *Opt. Express* **2022**, *30*, 42300–42307. [CrossRef] [PubMed]
7. Mirza, J.; Ghafoor, S.; Kousar, A.; Kanwal, B.; Qureshi, K.K. Design of a continuous-wave ytterbium-doped tunable fiber laser pump for thulium-doped fiber amplifiers. *Arab. J. Sci. Eng.* **2022**, *47*, 3541–3549. [CrossRef]
8. Martinez-Ramirez, L.G.; Silva-Alvarado, E.C.; Gallegos-Arellano, E.; Fernandez-Jaramillo, A.A.; Estudillo-Ayala, J.M.; Jauregui-Vazquez, D.; Rojas-Laguna, R.; Sierra-Hernandez, J.M. Select-cutoff Mach-Zehnder interferometer based on waist-enlarged technique and its multi-wavelength fiber laser application. *Infrared Phys. Technol.* **2023**, *128*, 104508. [CrossRef]
9. Mirza, J.; Ghafoor, S.; Atieh, A.; Kanwal, B.; Qureshi, K.K. Widely tunable and switchable multiwavelength erbium-doped fiber laser based on a single ring cavity. *J. Opt. Soc. Am. B* **2022**, *39*, 1118–1129. [CrossRef]
10. Zinnecker, V.; Madden, S.; Stokes-Griffin, C.; Compston, P.; Rode, A.V.; Rapp, L. Ultrashort pulse laser ablation of steel in ambient air. *Opt. Laser Technol.* **2022**, *148*, 107757. [CrossRef]
11. Zhang, Y.; Ito, Y.; Sun, H.; Sugita, N. Investigation of multi-timescale processing phenomena in femtosecond laser drilling of zirconia ceramics. *Opt. Express* **2022**, *31*, 37394–37406. [CrossRef]
12. Couto, F.A.; Paula, K.T.; Santos, M.V.; Ribeiro, S.J.L.; Mendonça, C.R. Direct femtosecond laser printing of silk fibroin periodic structure with lower mid-infrared reflectivity. *Opt. Mater.* **2022**, *135*, 113335. [CrossRef]
13. Flamm, D.; Kaiser, M.; Fell, M.; Kahmann, M.; Lang, M.; Kleiner, J.; Hesse, T. Protecting the edge: Ultrafast laser modified C-shaped glass edges. *J. Laser Appl.* **2022**, *34*, 012014. [CrossRef]
14. Yao, G.; Zhao, Z.; Liu, Z.; Gao, X.; Cong, Z. High repetition rate actively mode-locked Er:fiber laser with tunable pulse duration. *Chin. Opt. Lett.* **2022**, *20*, 071402. [CrossRef]
15. Lau, K.Y.; Perros, A.P.; Li, D.; Kim, M.; Sun, Z. Scalable graphene electro–optical modulators for all-fibre pulsed lasers. *Nanoscale* **2021**, *13*, 9873–9880. [CrossRef]
16. Set, S.Y.; Yaguchi, H.; Tanaka, Y.; Jablonski, M. Laser mode locking using a saturable absorber incorporating carbon nanotubes. *J. Light. Technol.* **2004**, *22*, 51–56. [CrossRef]
17. Sakakibara, Y.; Rozhin, A.G.; Kataura, H.; Achiba, Y.; Takumoto, M. Carbon nanotube-poly(vinylalcohol) nanocomposite film devices: Applications for femtosecond fiber laser mode lockers and optical amplifier noise suppressors. *Jpn. J. Appl. Phys.* **2005**, *44*, 1621–1625. [CrossRef]
18. Bao, Q.; Zhang, H.; Yang, J.; Wang, S.; Tang, D.Y.; Jose, R.; Ramakrishna, S.; Lim, C.T.; Loh, K.P. Graphene-polymer nanofiber membrane for ultrafast photonics. *Adv. Funct. Mater.* **2010**, *20*, 782–791. [CrossRef]
19. Sun, Z.; Hasan, T.; Torrisi, F.; Popa, D.; Privitera, G.; Wang, F.; Bonaccorso, F.; Basko, D.M.; Ferrari, A.C. Graphene mode-locked ultrafast laser. *ACS Nano* **2010**, *4*, 803–808. [CrossRef]
20. Yang, S.; Li, F.; Gong, M.-M.; Zhang, L.; Zhu, Z.-W.; Shen, H.-B.; Chen, S.-C. Generation of Q-switched and mode-locked pulses based on PbS/CdS saturable absorbers in an Er-doped fiber laser. *J. Mater. Chem. C* **2022**, *10*, 5956–5961. [CrossRef]
21. Sui, Z.; Yang, F.; Han, Y.; Fan, W.; Li, S.; Bai, C.; Lu, C.; Zhang, W.; Wang, G.; Fu, S.; et al. Large energy mode-locked phenomenon based on ZrS_2 in Er-doped fiber laser. *Opt. Laser Technol.* **2023**, *157*, 108725. [CrossRef]
22. Sohail, M.; Zhang, C.; Ahmed, R.; Asghar, H.; Khan, S.A.; Khan, N.Z.; Chen, T.; Baig, M.A.; Wang, Z. Carbon nanoparticles (CNPs) as a saturable absorber for a passively Q-switched erbium (Er^{3+}) doped fiber laser. *Opt. Laser Technol.* **2023**, *160*, 109046. [CrossRef]
23. Pawliszewska, M.; Tomaszewska, D.; Soboń, G.; Dużyńska, A.; Zdrojek, M.; Sotor, J. Broadband metallic carbon nanotube saturable absorber for ultrashort pulse generation in the 1500–2100 nm spectral range. *Appl. Sci.* **2021**, *11*, 3121. [CrossRef]
24. Soboh, R.S.M.; Al-Masoodi, A.H.H.; Erman, F.N.A.; Al-Masoodi, A.H.H.; Nizamani, B.; Arof, H.; Apsari, R.; Harun, S.W. Mode-locked ytterbium-doped fiber laser with zinc phthalocyanine thin film saturable absorber. *Front. Optoelectron.* **2022**, *15*, 28. [CrossRef] [PubMed]
25. Sahib, M.A.A.B.; Zulkipli, N.F.; Rosol, A.H.A.; Yasin, M.; Harun, S.W. Titanium carbide MXene as a mode locker in erbium-doped fiber laser cavity. *J. Russ. Laser Res.* **2022**, *43*, 328–333. [CrossRef]
26. Pang, L.; Zhao, M.; Zhao, Q.; Li, L.; Wang, R.; Wu, R.; Lv, Y.; Liu, W. GaSb film is a saturable absorber for dissipative soliton generation in a fiber laser. *ACS Appl. Mater. Interfaces* **2022**, *14*, 55971–55978. [CrossRef]
27. Wang, P.; Zhu, C.; Sun, Y.; Zhao, Y. Mode-locked fiber laser based on α-Fe_2O_3 nanosheets as saturable absorbers. *Opt. Laser Technol.* **2021**, *144*, 107417. [CrossRef]
28. Omar, S.; Zulkipli, N.F.; Ahmed, N.; Jusoh, Z.; Musa, B.; Apsari, R.; Harun, S.W. Lanthanum hexaboride for Q-switching and mode-locking applications. *Opt. Commun.* **2022**, *502*, 127396. [CrossRef]
29. Martinez, A.; Fuse, K.; Xu, B.; Yamashita, S. Optical deposition of graphene and carbon nanotubes in a fiber ferrule for passive mode- locked lasing. *Opt. Express* **2010**, *18*, 23054–23061. [CrossRef]
30. Nicholson, J.W.; Windeler, R.S.; DiGiovanni, D.J. Optically driven deposition of single-walled carbon-nanotube saturable absorbers on optical fiber end-faces. *Opt. Express* **2007**, *15*, 9176–9183. [CrossRef]
31. Kashiwagi, K.; Yamashita, S. Optically manipulated deposition of carbon nanotubes onto optical fiber end. *Jpn J. Appl. Phys.* **2007**, *46*, L988–L990. [CrossRef]
32. Novoselov, K.S.; Geim, A.K.; Morozov, S.V.; Jiang, D.; Zhang, Y.; Dubonos, S.V.; Grigorieva, I.V.; Firsov, A.A. Electric field effect in atomically thin carbon films. *Science* **2004**, *306*, 666–669. [CrossRef]
33. Geim, A.K.; Novoselov, K.S. The rise of graphene. *Nat. Mater.* **2007**, *6*, 183–191. [CrossRef] [PubMed]

34. Chang, Y.M.; Kim, H.; Lee, J.H.; Song, Y.W. Multilayered graphene efficiently formed by mechanical exfoliation for nonlinear saturable absorbers in fiber mode-locked lasers. *Appl. Phys. Lett.* **2010**, *97*, 211102. [CrossRef]
35. Chen, Y.; Jiang, G.; Chen, S.; Guo, Z.; Yu, X.; Zhao, C.; Zhang, H.; Bao, Q.; Wen, S.; Tang, D.; et al. Mechanically exfoliated black phosphorus as a new saturable absorber for both Q-switching and mode-locking laser operation. *Opt. Express* **2015**, *23*, 12823–12833. [CrossRef] [PubMed]
36. Sotor, J.; Sobon, G.; Kowalczyk, M.; Mzcherzynski, W.; Paletko, P.; Abramski, K.M. Ultrafast thulium-doped fiber laser mode locked with black phosphorus. *Opt. Lett.* **2015**, *40*, 3885–3888. [CrossRef]
37. Yu, X.; Yu, P.; Wu, D.; Singh, B.; Zeng, Q.; Lin, H.; Zhou, W.; Lin, J.; Suenaga, K.; Liu, Z.; et al. Atomically thin noble metal dichalcogenide: A broadband mid-infrared semiconductor. *Nat. Commun.* **2018**, *9*, 1545. [CrossRef]
38. Steinberg, D.; Zapata, J.D.; Nascimento, R.; Rosa, H.G.; Saito, L.A.M.; Thoroh de Souza, E.A. Mode-locked erbium-doped fiber laser based on a mechanically exfoliated ReS_2 saturable absorber onto D-shaped optical fiber. *Opt. Express* **2022**, *12*, 4506–4517. [CrossRef]
39. Ooi, S.I.; Ahmad, H. Thermal release tape assisted mechanical exfoliation of pristine TMD and the performance of the exfoliated TMD saturable absorbers for Q-switched laser generation. *Opt. Mater.* **2022**, *128*, 112363. [CrossRef]
40. Li, J.; Wang, L.; Chen, Y.; Li, Y.; Zhu, H.; Li, L.; Tong, L. Interfacial charge transfer and ultrafast photonics application of 2D graphene/InSe heterostructure. *Nanomaterials* **2023**, *13*, 147. [CrossRef]
41. Zhu, G. Graphene mode-locked fiber laser at 2.8 μm. *IEEE Photon. Technol. Lett.* **2016**, *28*, 7–10. [CrossRef]
42. Hai, T.; Xie, G.; Qiao, Z.; Qin, Z.; Ma, J.; Sun, Y.; Wang, F.; Yuan, P.; Ma, J.; Qian, L. Indium selenide film: A promising saturable absorber in 3- to 4-μm band for mid-infrared pulsed laser. *Nanophotonics* **2020**, *9*, 2045–2052. [CrossRef]
43. Qin, Z.; Hai, T.; Xie, G.; Ma, J.; Yuan, P.; Qian, L.; Li, L.; Zhao, L.; Shen, D. Black phosphorus Q-switched and mode-locked mid-infrared Er:ZBLAN fiber laser at 3.5 μm wavelength. *Opt. Express* **2018**, *26*, 8224–8231. [CrossRef] [PubMed]
44. Wei, J.; Li, P.; Yu, L.; Ruan, S.; Li, K.; Yan, P.; Wang, J.; Wang, J.; Guo, C.; Liu, W.; et al. Mode-locked fiber laser of 3.5 μm using a single-walled carbon nanotube saturable absorber mirror. *Chin. Opt. Lett.* **2022**, *20*, 011404. [CrossRef]
45. Lau, K.Y.; Latif, A.A.; Abu Bakar, M.H.; Muhammad, F.D.; Huang, N.M.; Omar, M.F.; Mahdi, M.A. Passively mode-locked ultrashort pulsed fiber laser incorporating multi-layered graphene nanoplatelet saturable absorber. *J. Phys. Commun.* **2018**, *2*, 075005. [CrossRef]
46. Abas, A.F.; Lau, K.Y.; Muhammad, F.D.; Abdulkawi, W.M.; Al-Moliki, Y.M.; Alresheedi, M.T.; Mahdi, M.A. Dual-wavelength mode-locked oscillation with graphene nanoplatelet saturable absorber in erbium-doped fiber laser. *Electronics* **2022**, *11*, 2880. [CrossRef]
47. Hamra, A.A.B.; Lim, H.N.; Chee, W.K.; Huang, N.M. Electro-exfoliating graphene from graphite for direct fabrication of supercapacitor. *Appl. Surf. Sci.* **2016**, *360*, 213–223. [CrossRef]
48. Liu, G.X.; Feng, D.J.; Zhang, M.S.; Jiang, S.Z.; Zhang, C. Mode-locked erbium-doped all fiber laser using few-layer graphene as a saturable absorber. *Opt. Laser Technol.* **2015**, *72*, 70–73. [CrossRef]
49. Xu, H.; Wan, X.; Ruan, Q.; Yang, R.; Du, T.; Chen, N.; Cai, Z.; Luo, Z. Effects of nanomaterial saturable absorption on passively mode-locked fiber lasers in an anomalous dispersion regime: Simulations and experiments. *IEEE J. Sel. Top. Quantum Electron.* **2018**, *24*, 1100209. [CrossRef]
50. Giles, C.R.; Desurvire, E. Modeling of erbium-doped fiber amplifier. *J. Light. Technol.* **1991**, *9*, 271–283. [CrossRef]